Antarctic Bottom Water Warming and Freshening: Contributions to Sea Level Rise, Ocean Freshwater Budgets, and Global Heat Gain*

SARAH G. PURKEY

School of Oceanography, University of Washington, and NOAA/Pacific Marine Environmental Laboratory, Seattle, Washington

GREGORY C. JOHNSON

NOAA/Pacific Marine Environmental Laboratory, and School of Oceanography, University of Washington, Seattle, Washington

(Manuscript received 27 November 2012, in final form 8 February 2013)

ABSTRACT

Freshening and warming of Antarctic Bottom Water (AABW) between the 1980s and 2000s are quantified, assessing the relative contributions of water-mass changes and isotherm heave. The analysis uses highly accurate, full-depth, ship-based, conductivity–temperature–depth measurements taken along repeated oceanographic sections around the Southern Ocean. Fresher varieties of AABW are present within the South Pacific and south Indian Oceans in the 2000s compared to the 1990s, with the strongest freshening in the newest waters adjacent to the Antarctic continental slope and rise indicating a recent shift in the salinity of AABW produced in this region. Bottom waters in the Weddell Sea exhibit significantly less water-mass freshening than those in the other two southern basins. However, a decrease in the volume of the coldest, deepest waters is observed throughout the entire Southern Ocean. This isotherm heave causes a salinification and warming on isobaths from the bottom up to the shallow potential temperature maximum. The water-mass freshening of AABW in the Indian and Pacific Ocean sectors is equivalent to a freshwater flux of 73 ± 26 Gt yr^{-1}, roughly half of the estimated recent mass loss of the West Antarctic Ice Sheet. Isotherm heave integrated below 2000 m and south of 30°S equates to a net heat uptake of 34 ± 14 TW of excess energy entering the deep ocean from deep volume loss of AABW and 0.37 ± 0.15 mm yr^{-1} of sea level rise from associated thermal expansion.

1. Introduction

Antarctic Bottom Water (AABW) is the Southern Ocean's coldest, densest water mass. It ventilates the lower limb of the meridional overturning circulation (MOC; e.g., Lumpkin and Speer 2007), filling most of the world's deep basins (Johnson 2008). In recent decades, AABW has warmed (e.g., Purkey and Johnson 2010, hereafter PJ10), freshened (e.g., Johnson et al. 2008; Swift and Orsi 2012), and decreased in volume (e.g., Kouketsu et al. 2011; Purkey and Johnson 2012, hereafter PJ12), possibly linked to the increase in the glacial melt freshwater fluxes into AABW formation regions around Antarctica (e.g., Jacobs and Giulivi 2010). The freshening decreases the salinity of the shelf waters, thence AABW, and appears to slow AABW production and thus the lower limb of the MOC. Here we examine AABW property changes throughout the Southern Ocean, separating the component owing to potential temperature–salinity (θ–S) changes from that due to changes in the depth of potential isotherms (heave). Heave reflects changes in AABW volume, related to changes in the formation rate, circulation, or perhaps even formation properties of AABW. A shift in the θ–S curve indicates a change in water-mass properties. Decomposing the observed deep changes into these components allows for evaluation of the relative contributions of these changes to local sea level rise (SLR), freshwater, and heat budgets.

AABW is a combination of very cold and relatively fresh water formed on shallow continental shelves and warmer, saltier offshore Circumpolar Deep Water (CDW; Foster and Carmack 1976). The shelf waters form on shallow ice-covered continental shelves where brine

* Pacific Marine Environmental Laboratory Contribution Number 3954.

Corresponding author address: Sarah G. Purkey, School of Oceanography, Box 357940, University of Washington, Seattle, WA 98195-7940.
E-mail: sarah.purkey@noaa.gov

DOI: 10.1175/JCLI-D-12-00834.1

rejection from sea ice formation and export increases the salinity of surface waters. This water sinks, mixing with adjacent CDW, and circulates under the ice shelf, melting the overlying ice at depth, causing the shelf waters to freshen (Jacobs 2004). These processes result in a reservoir of very cold, dense shelf water that, when it leaves the shelf, flows down the continental slope, further mixing with CDW (Jacobs 2004).

AABW formation occurs in the Ross Sea, Adelie coast, and Weddell Sea, producing at least three distinct varieties of AABW (Orsi et al. 1999): Ross Sea Bottom Water (RSBW), Adelie Land Bottom Water (ALBW), and Weddell Sea Bottom Water (WSBW). These water masses mix with overlying CDW in the Antarctic Circumpolar Current (ACC) before feeding into the lower limb of the MOC and traveling to the northern ends of the Pacific, west Atlantic, and Indian Oceans (Johnson 2008). AABW is often defined as water with neutral density $\gamma_n > 28.27\,\mathrm{kg\,m^3}$ found south of the Subantarctic Front (SAF; Orsi et al. 1999). Here we use an older definition for AABW of deep Southern Ocean waters of $\theta < 0°\mathrm{C}$ (e.g., Gordon 1972), because we use θ, rather than γ_n, as a vertical coordinate.

AABW freshening has been observed (Aoki et al. 2005; Jacobs and Giulivi 2010; Swift and Orsi 2012) and slowdown of AABW formation rates inferred (PJ12) in the Ross Sea and Australian–Antarctic basin starting as early as the 1950s. Ross Sea Shelf Water, an important constituent of RSBW, has freshened by $0.03\,\mathrm{decade^{-1}}$ between 1958 and 2008 [here salinity is reported on the 1978 Practical Salinity Scale (PSS-78), a dimensionless scale derived from the conductivity of the sampled seawater]. This freshening is associated with freshening of the coastal current connecting the Amundsen coast to the Ross Sea Shelf (Jacobs and Giulivi 2010). Along the west side of the Ross gyre, within the deep western boundary current transporting the recently formed RSBW northwestward, the densest water seen in 1994 completely disappeared by 2011, the deep and surface constituents of the shelf water freshened, and thickness of the RSBW outflow decreased by a few hundred meters (Swift and Orsi 2012). Directly downstream from its formation region in the Australian–Antarctic basin, ALBW has freshened by 0.03 PSS-78 between 1994 and 2002 (Aoki et al. 2005). In the deep Australian–Antarctic basin, ventilated by both RSBW and ALBW, freshening is evident throughout the basin, owing either to fresher bottom water or different ratios of RSBW and ALBW (Whitworth 2002; Rintoul 2007; Johnson et al. 2008). In both the Australian–Antarctic basin and the Ross Sea, cooling on isopycnals and warming on isobars are also present (Aoki et al. 2005; Johnson et al. 2008; Jacobs and Giulivi 2010; PJ10).

In the Weddell Sea, bottom water and deep water have been warming with little change in salinity (Robertson et al. 2002; Fahrbach et al. 2004, 2011; PJ10). To the north, the deep waters in the Scotia Sea and Argentine Basin, both directly fed by WSBW, have warmed and decreased in volume for at least the past three decades (Coles et al. 1996; Johnson and Doney 2006; Meredith et al. 2008; PJ12).

Outside the Southern Ocean, the abyssal waters along the bottom limb of the MOC fed by AABW (Johnson 2008) have warmed around the globe (PJ10; Kouketsu et al. 2011). The global-scale warming could be caused by a decrease in AABW formation rates, causing isopycnals to fall: hence, the observed warming on isobaths. This signal can be communicated remotely by planetary waves throughout the World Ocean on much shorter time scales than advective changes (Masuda et al. 2010; Kouketsu et al. 2011; PJ12). AABW warming has been analyzed in the western South Atlantic (Johnson and Doney 2006; Zenk and Morozov 2007), throughout the Pacific (Fukasawa et al. 2004; Johnson et al. 2007; Kawano et al. 2010), and in the eastern Indian Ocean (Johnson et al. 2008; PJ10).

Much of the recent AABW property changes observed around the globe may be owing to increased glacial freshwater discharge from a number of locations around Antarctica over recent decades (e.g., Jacobs and Giulivi 2010). Antarctic ice shelf thinning and glacial discharge acceleration are strongest along the West Antarctic Peninsula and the Amundsen coast (Rignot and Jacobs 2002; Rignot et al. 2008), with a net ice sheet loss of $88 \pm 54\,\mathrm{Gt\,yr^{-1}}$ in the West Antarctic and $60 \pm 46\,\mathrm{Gt\,yr^{-1}}$ along the peninsula between 1992 and 2006 (Rignot et al. 2008). Between 1991 and 2001, $154 \pm 16\,\mathrm{km^3}$ of glacier ice was lost to the Amundsen Sea with acceleration of coastward glacier flow (Shepherd et al. 2002). At Pine Island Glacier, a location with one of the highest melt rates, the ice shelf has recently been thinning at a rate of $5.5\,\mathrm{m\,yr^{-1}}$ through basal melting because of a 0.5°C warming of ocean waters under the ice shelf (Shepherd et al. 2004). Similarly, along the Amundsen and Bellingshausen coasts where warm CDW has access to the shelf, the melting rates on the submerged undersides of glaciers have been correlated with warming ocean temperatures, with melting increasing by $1\,\mathrm{m}\,(0.1°\mathrm{C})^{-1}$ of warming (Rignot and Jacobs 2002).

The observed AABW property and circulation changes are important for global heat and SLR budgets (PJ10; Kouketsu et al. 2011). The deep-ocean warming below 4000 m globally is equivalent to a net heat uptake of $0.027 \pm 0.009\,\mathrm{W\,m^{-2}}$ over the surface of the earth and $0.05\,\mathrm{mm\,yr^{-1}}$ mean global SLR (PJ10). In the Southern Ocean, the warming below 1000 m is equivalent to as

much as a 1.2 W m^{-2} local heat flux and 1.3 mm yr^{-1} local SLR (PJ10).

Here we evaluate salinity and temperature changes within the deep Southern Ocean, distinguishing between heave and water property changes. Section 2 discusses the dataset and processing, including intercruise salinity adjustments (see also the appendix). Section 3 presents methods used to distinguish heave from water-mass changes. Section 4 discusses freshening trends throughout the Southern Ocean, using multiple Southern Ocean sections occupied two or more times since the 1980s. Section 5 estimates basin-mean rates of change to find the contributions of the deep Southern Ocean to changes in SLR, heat budgets, and freshwater budgets. Section 6 discusses these results.

2. Data and processing

We use full-depth, high-resolution, highly accurate, ship-based hydrographic data collected in the Southern Ocean since 1980 at locations with two or more occupations. The data were mostly collected as part of the international World Ocean Circulation Experiment (WOCE) Hydrographic Programme or the Global Ocean Ship-Based Hydrographic Investigation Program (GO-SHIP). All publicly available data (at http://cchdo.ucsd.edu) as of November 2012 are considered here. We refer to each section by its WOCE identification (ID; Fig. 1 and Table A1). All data collected along a section within a year are combined and referred to as a single occupation of that section, referenced by the calendar year in which the earliest station was taken (Table A1).

We focus on sections located at or south of 30°S (Fig. 1): nine meridional sections roughly spaced every 45° longitude, two zonal sections at ~67°S across the Ross Sea and the Weddell Sea, and three zonal sections that together completely circumnavigate the globe near 30°S. Most of the meridional sections in the Indian and Atlantic Ocean sectors extend to the Antarctic continental shelf, but both of the sections in the Pacific sector stop short of the shelf (Fig. 1). Along each section data were collected from the surface to approximately 10 m from the bottom at stations nominally spaced every 55 km. Each reoccupation of a given section analyzed here lies within 10 km of the original. Data along each section are interpolated onto an evenly spaced 20-dbar vertical and 2′ horizontal grid following PJ10.

Data were collected between 1980 and 2012, with the length-weighted mean first occupation in 1991 and the last in 2008. Each section has been occupied between two and eight times with the length-weighted mean and median for the study region of 3.6 and 3.0 occupations, respectively (Table A1). Therefore, the along-section trends discussed here span on average an 18-yr period. Most trend estimates are based on data from at least three occupations; however, some trends are based on the difference between two occupations (Table A1).

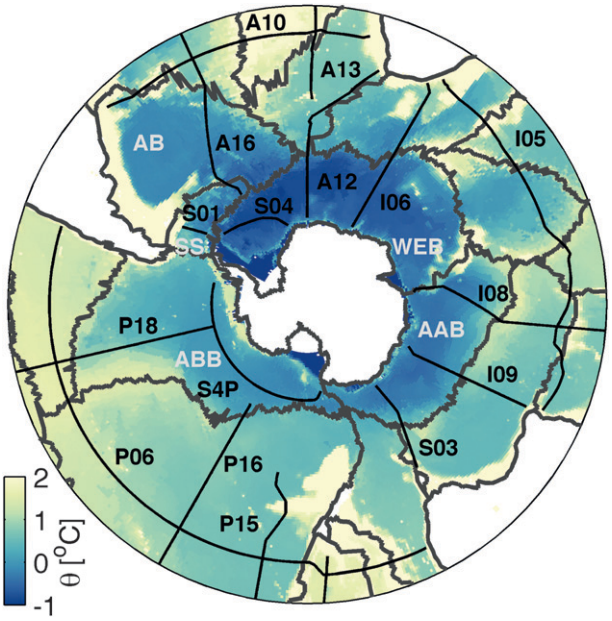

FIG. 1. Southern Ocean section locations (black lines) labeled with WOCE IDs (black characters) and basin boundaries (gray lines) over bottom potential temperature (color shading; Gouretski and Koltermann 2004) with land (white areas). Basin names (white characters) are indicated by abbreviations including the following: Weddell–Enderby basin (WEB), Australian–Antarctic basin (AAB), Amundsen–Bellingshausen basin (ABB), Scotia Sea (SS), and the Argentine Basin (AB).

All data were collected with a conductivity–temperature–depth (CTD) instrument with target measurement accuracy better than 0.002°C for temperature, 3 dbar for pressure, and 0.002 PSS-78 for salinity (Joyce 1991). All CTD temperature data were reported in or converted to the 1968 International Practical Temperature Scale (IPTS-68) for use with the 1980 Equation of State (EOS-80). The CTD salinity measurements were all standardized with International Association for Physical Science of the Oceans (IAPSO) Standard Seawater (SSW), with all salinity values reported here on PSS-78. We consider only data with good quality flags and remove any obvious spikes in salinity data.

We apply known salinity offsets owing to the different IAPSO SSW batches used on the different cruise legs to the salinity data (Table A1). Batch-to-batch offsets are from Kawano et al. (2006) and T. Kawano (2011, personal communication). They range from -1.2×10^{-3} to 2.5×10^{-3} PSS-78 (Table A1). SSW offsets could not be applied to 13 of the 73 Southern Ocean cruise legs analyzed here because of 8 legs having no SSW batch number

information available and 5 cruises using SSW batches too recent to have an offset estimate.

Additional ad hoc salinity adjustments are estimated and applied to the CTD salinity data to further minimize intercruise measurement biases (see appendix: Table A1 and Fig. A1). These salinity offsets are calculated by comparing salinity data in select geographical regions containing water that has been isolated from the surface for a relatively long time and is hence well-mixed with a very tight (low variance) θ–S relation (see appendix). These additional offsets are necessary because of the relatively large contribution of salinity to density and the relatively high ratio of measurement error to signal observed here (see appendix).

The ad hoc salinity offsets are applied to 67 of the 73 Southern Ocean legs with magnitudes ranging from essentially zero ($<10^{-6}$ PSS-78) to as high as 0.0056 PSS-78, with 63 of the applied offsets being less than the WOCE target accuracy of 0.002 PSS-78 (Fig. A1). The four legs with offset magnitudes >0.002 PSS-78 are the 1984 occupation of P16, the 1993 and 1995 occupations of S03, and the 2011 occupation of A16 (Fig. A1; Table A1). A salinity offset could not be applied to six legs. These legs include the three occupations of S01 through the Drake Passage (Fig. 1), where highly variable water properties did not allow a suitable place for intercruise comparisons. Also three subsections of full lines are not long enough for salinity comparisons: namely, the 1995, 2006, and 1991 occupations of I09, P18, and S03, respectively. The salinity offsets are applied to the raw CTD salinity data and each section occupation is regridded vertically and horizontally (PJ10).

3. Methods: Heave versus water property changes

Interior ocean property changes can be caused by heave or water-mass changes (e.g., Fig. 2). A number of methods have been used for distinguishing between heave and water-mass changes. For example, Bindoff and McDougall (1994) decompose ocean property changes using S and θ changes on both density and pressure surfaces and the original θ–S curve to solve for the contributions of isopycnal heave, temperature changes, and salinity changes, whereas McDonagh et al. (2005) calculate water-mass changes by calculating the ''minimum distance'' between chronological θ–S curves, scaling them by thermal expansion and haline contraction coefficients.

Here we use θ as the independent variable instead of density to allow detection of very small deep θ–S changes. We make this choice because S errors have significantly more impact on density than θ errors, especially in cold deep waters. For example, at 4000 m in the Ross Sea, the expected measurement salinity error

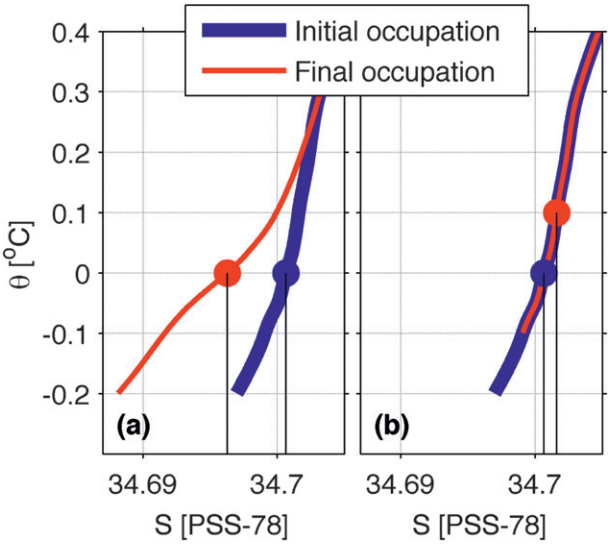

FIG. 2. Schematics of changes in salinity between an initial (blue) and final (red) occupation of a given station owing to (a) water-mass change and (b) isotherm heave. Water-mass changes in (a) can be seen as a change in the θ–S curve causing a deep freshening signal between occupations (black lines) at the same depths (dots). Isotherm heave in (b), caused by a vertical displacement of potential isotherms, causes water at the same depth (dots) to warm and become more saline between occupations (black lines).

of 0.002 PSS-78 will cause an error in density 15 times larger than the expected temperature error of 0.001°C would cause. Therefore, we choose the most accurate measurement, θ, to be the independent variable in our analysis, rather than density, which would amplify any remaining S errors.

As a result of this choice, here heave refers to a vertical shift of the water column caused by a change in depth (equivalently pressure) of a potential isotherm that has no effect on the local θ–S relationship (Fig. 2b). Alternatively, a water-mass change is reflected in a shift in the shape of the θ–S curve with time (e.g., Fig. 2a). If density surfaces were used as the vertical coordinate, water-mass and heave changes reported here would be amplified, as salinity generally decreases with decreasing temperature within AABW in the Southern Ocean.

While this method clearly identifies where θ–S changes occur, it casts all the water-mass changes in terms of salinification (or freshening) and all warming (or cooling) as owing to heave. For example, imagine a scenario in the deep Southern Ocean (where θ decreases and S increases with increasing depth) where the whole water column warms, causing the θ–S curve to be displaced upward. Our analysis would cast this water-mass change as freshening, with a value proportional to the warming by the local slope of the θ–S curve. While deep AABW freshening presented here is traced back to the shelf

water changes that are freshening faster than warming (e.g., Jacobs and Giulivi 2010), the limitations of our method should be kept in mind.

To decompose the deep property changes, first we define an initial θ–S relation (θ–S_i) representative of the θ–S at the time of the first occupation at every location along a section. Each vertical profile of S and θ of each section is linearly interpolated onto an evenly spaced θ grid from $-2°$ to 5°C at 0.01°C intervals. The interpolation extends from the bottom to the first θ maximum (usually the θ maximum associated with CDW). All values above the maximum are masked out. The bottom S value of each interpolated S profile is extended to the minimum bottom θ measured at that location among all occupations of the section by using the slope of the linear fit of S versus θ over the coldest 0.1°C of each profile. This extension is only applied if the bottom $\theta < 3$°C, the profile depth > 500 m, and the bottom 0.1°C spans more than 100 m of the water column. These criteria limit extensions to deeper offshore regions, excluding thermocline or continental shelf waters. Finally, S_i at each θ grid is estimated for the time of the first occupation from linear fits of S versus time for all occupations. If there are only two occupations, then S_i matches S of the first occupation but, if there are multiple occupations of a section, then S_i will differ from S of the first occupation.

The θ–S_i relations are used to calculate expected S values S_H if heave were the only contributor to the changes in S. At each vertical and horizontal gridpoint for each occupation, a value of S_H is computed from θ using a spline interpolant and the local θ–S_i relation.

Finally, we calculate S rates of change for the total S_T, S_H, and water-mass shift S_{WM} with time and associated error as follows: At every horizontal and vertical grid point along each section with at least two occupations spanning more than 2.5 yr (following PJ10), the rate of change of total S with time dS_T/dt and dS_H/dt are estimated by linear least squares (e.g., Fig. 3). Where only two occupations exist, the rates of change reflect differences between these two occupations. Within the Southern Ocean below 300 m, the trend error along sections with more than two occupations is usually less than 0.4×10^{-3} PSS-78 yr^{-1}, smaller than most of the along-section signal (e.g., Fig. 3). The rate of change in salinity with time owing to water-mass shifts, $dS_{\mathrm{WM}}/dt = dS_T/dt - dS_H/dt$, is calculated along each section (e.g., Figs. 3a,d,g,j,m). In addition, the rate of change of θ with time $d\theta/dt$ is found also using a linear least squares fit (not shown; see PJ10).

For each deep basin (following PJ12; Fig. 1), the rates along all sections within a given basin are used to find basin-mean rates and associated errors within 0.05°C-thick bins below 5°C. Along each section within a basin, using the mean θ from all occupations, a θ bin is identified as the region where θ falls within ± 0.025°C of a given value. Within each θ-bin area, first the vertical mean $d\theta/dt$, dS_T/dt, dS_{WM}/dt, and dS_H/dt are calculated along the sections. The vertical length of the given θ bin at each location along the section is used to find a horizontal length-weighted mean rate (basin-mean rates) for each θ bin using all sections within a basin as if they were lined up end to end. The horizontal variance along a θ bin is much larger than the vertical variance within a θ bin. Therefore, we calculate and use the horizontal standard deviation of the vertical mean rates along a given isotherm (basin standard deviations) for the basin error analyses. The basin standard deviations are also calculated as if all sections within a basin were connected end to end, a more conservative choice than the section length-weighted mean technique used in PJ10. In addition, the basin standard deviations are usually larger than the slope errors on the rates themselves. Slope errors are neglected in the final error analysis since they cannot be determined for most sections. Finally, the degrees of freedom (DOF) for each isotherm bin are calculated using the horizontal length of the θ bin following PJ10, assuming a 163-km decorrelation length scale (PJ10). The 95% confidence intervals are found for each basin for each θ bin assuming a Student's t distribution (e.g., Fig. 4).

The 95% confidence intervals reported here are based on the spatial variance of trends along the sections and do not fully resolve the error associated with temporal variability in the trend. However, as noted earlier, the trend errors in time along sections with more than two occupations (the majority of the sections analyzed) are generally smaller than the signal. In addition, the consistent patterns seen throughout the Southern Ocean in all sections analyzed (section 4), all occupied over varying time periods, increases confidence that the basin-mean rates reported here reflect a fairly consistent decadal change, at least from the 1980s through the 2000s. Furthermore, in the few areas with better temporal sampling, fairly steady AABW warming has been observed over the past few decades (e.g., Zenk and Morozov 2007). However, to resolve fully the temporal variability and determine if the changes are associated with a secular trend or an oscillation or have a more complex temporal pattern over the 30-yr reporting period would require a higher-temporal-resolution large-scale dataset.

4. Results

Throughout the Southern Ocean, water colder than 0°C in each of the deep basins is freshening because of

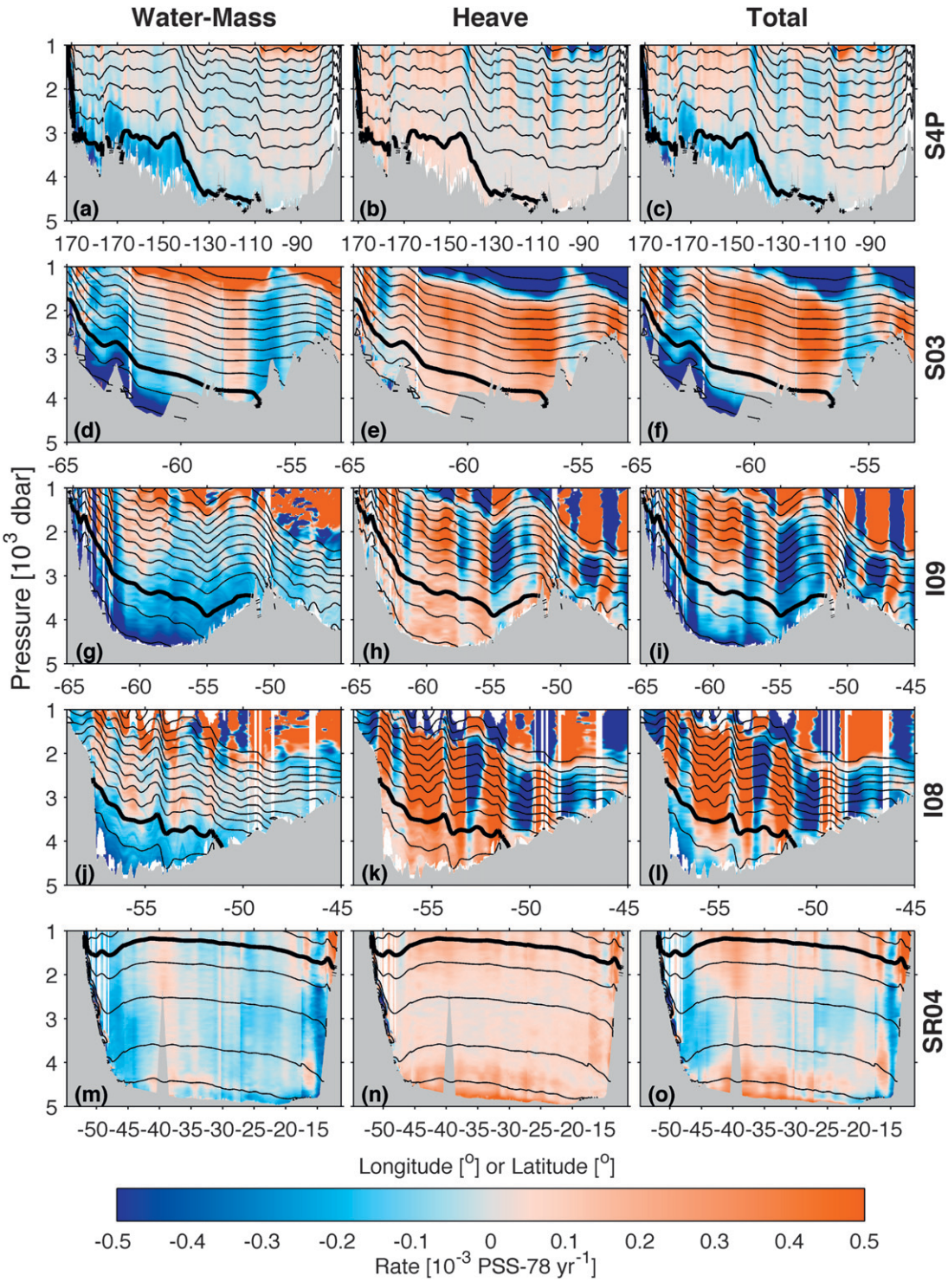

FIG. 3. Rate of change in S (color; PSS-78 yr^{-1}) vs pressure and latitude or longitude along (a)–(c) S4P, (d)–(f) S03 across the Australian–Antarctic basin, (g)–(i) I09 across the Australian–Antarctic basin, (j)–(l) I08 across the Australian–Antarctic basin, and (m)–(o) SR04 across the Weddell Sea (see Fig. 1 for locations). Orange indicates areas of salinification and blue areas of freshening with mean isotherms contoured at 0.2°C intervals (thin black lines; 0°C isotherm is the thick black line). The (a),(d),(g),(j),(m) water-mass and (b),(e),(h),(k),(n) heave contributions to (c),(f),(i),(l),(o) the total are separated.

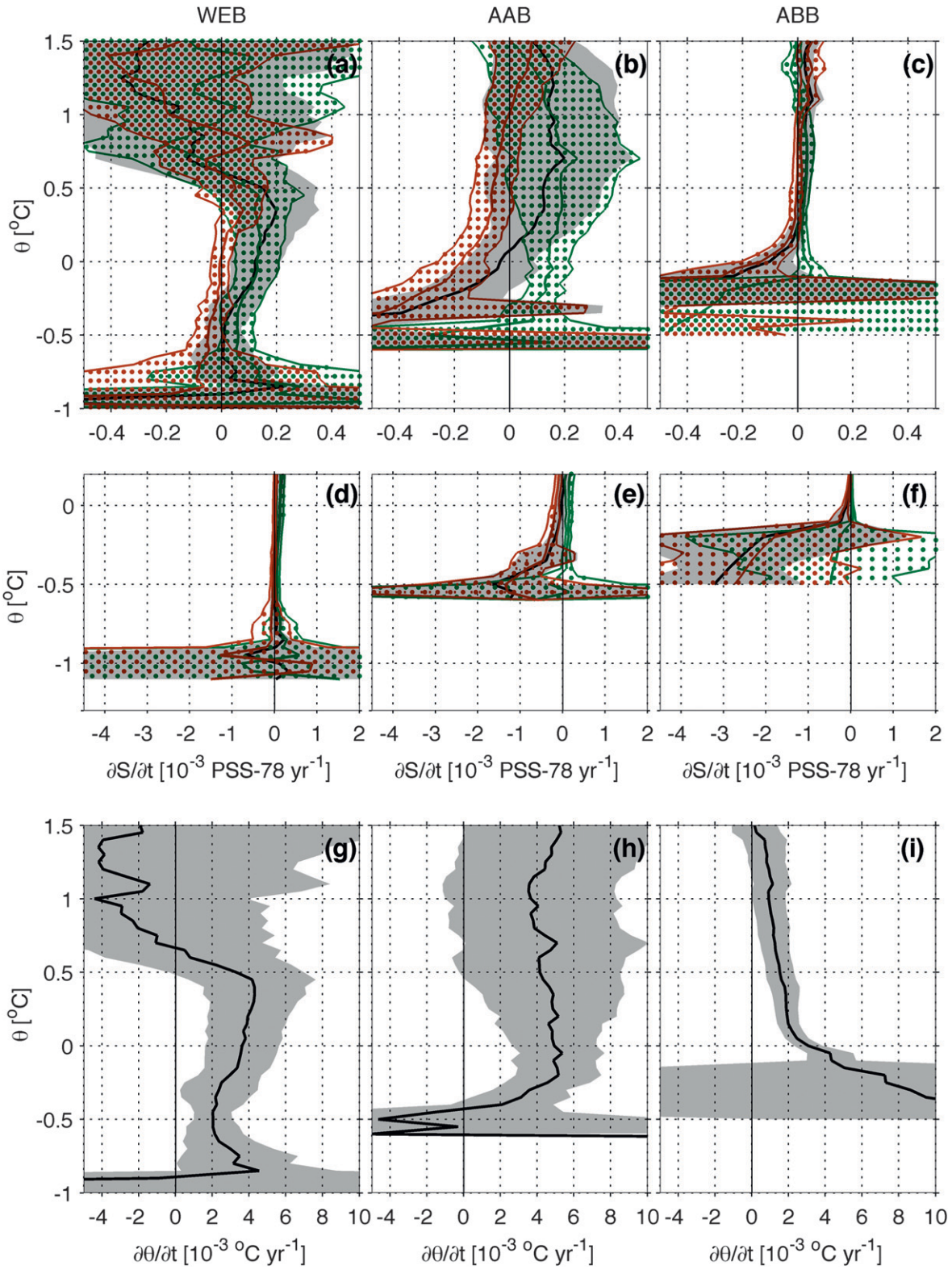

FIG. 4. Basin-mean rates of change in (a)–(f) S (black; PSS-78 yr^{-1}) and (g)–(i) θ (black; °C yr^{-1}) with 95% confidence intervals (gray shading) estimated along time-mean θ surfaces in the WEB, AAB, and ABB (see Fig. 1). The water-mass (red) and heave (green) contributions to the total with 95% confidence intervals (dots) are shown over a large θ range (a)–(c) to show interior changes and are vertically expanded over a limited θ range (d)–(f) to show large changes found in the coldest waters along the continental slope (see Fig. 3).

water-mass changes, albeit in varying amounts, and becoming saltier below the CDW S maximum because of heave. The net effect is a deep freshening in the Indian and Pacific Oceans below 0°C with salinification above (Figs. 3a–l, 4b,c). In the South Atlantic, heave dominates to effect a nearly full water column salinification (Figs. 3m–o, 4a).

In the South Pacific, water-mass freshening dominates the total S signal in waters of $\theta < 0$°C throughout the Ross gyre (west of 140°W; Figs. 3a–c), with freshening increasing by an order of magnitude to 3 (± 2) $\times 10^{-3}$ PSS-78 yr^{-1} in the waters along the continental rise on the western side of the basin where the purest and most recently formed RSBW flows northwestward (Jacobs and Giuivi 2010). This strongest freshening along the continental rise in the coldest waters ($\theta < -0.4$°C) is almost completely due to water-mass shifts (Fig. 4f) and is consistent with the total freshening reported by Swift and Orsi (2012) in this region. Within the interior of the Ross gyre, water-mass freshening is $\sim 0.2 \times 10^{-3}$ PSS-78 yr^{-1} for $\theta < 0$°C (Figs. 3a, 4c). The heave component causes an $\sim 0.03 \times 10^{-3}$ PSS-78 yr^{-1} salinification between the bottom and 1000 m (Figs. 3b, 4c) because of a reduction in the volume of the coldest bottom waters, significantly different from zero at 95% confidence in the basin mean for 0.2°C $< \theta <$ 0.9°C. These two counteracting factors combine such that water-mass freshening dominates for $\theta < 0$°C, with a net freshening of 0.16×10^{-3} PSS-78 decade^{-1}, while heave dominates between 0°C and 1000 m, causing a net salinification (Figs. 3c, 4c,f). The Amundsen Basin (east of 140°W) exhibits a slight water-mass freshening and heave salinification for zero net change in salinity along S4P (Figs. 3a–c) and in the two meridional sections that cross the basin (Fig. 1; not shown).

In the south Indian Ocean, water-mass freshening is present throughout AABW (Figs. 3d,g,j) and strongest along the continental slope, where recently formed RSBW and ALBW flow westward before flowing north, ventilating the deep Australian–Antarctic basin (Orsi et al. 1999). Consistent with previous studies (Aoki et al. 2005; Rintoul 2007; Johnson et al. 2008; Jacobs and Giuivi 2010; Shimada et al. 2012), our results show a strong water-mass freshening, with basin-mean rates ranging from 1.2 (± 0.6) $\times 10^{-3}$ PSS-78 yr^{-1} within the coldest ($\theta \sim -0.5$°C) bottom water to 0.2 (± 0.1) $\times 10^{-3}$ PSS-78 yr^{-1} at $\theta = 0$°C (Figs. 4b,e). The freshening signal in the bottom waters ($\theta < -0.2$°C) becomes gradually fainter from west to east: starting at $\sim 0.6 \times 10^{-3}$ PSS-78 yr^{-1} in S03 (Fig. 3d, ~140°E) to $\sim 0.5 \times 10^{-3}$ PSS-78 yr^{-1} in I09 (Fig. 3g, ~115°E) to $\sim 0.3 \times 10^{-3}$ PSS-78 yr^{-1} in I08 (Fig. 3j, ~90°E). Again, heave partially counteracts this freshening in all sections (Figs. 3e,h,k). The basin-mean dS_H/dt accounts for $\sim 0.15 \times 10^{-3}$ PSS-78 yr^{-1} of salinification, statistically significantly different from zero for -0.3°C $< \theta <$ 0.5°C (Figs. 4b,e). The basin-mean dS/dt shows a net freshening for $\theta <$ 0°C and mostly a net salinification for $\theta >$ 0°C (Figs. 3f,i,l, 4b,e).

In the South Atlantic, less water-mass freshening is observed with more heave salinification, causing a very slight, and statistically insignificant net salinification of ~ 0.1 (± 0.13) $\times 10^{-3}$ PSS-78 yr^{-1} throughout the deep waters ($\theta < 0.4$°C; e.g., Figs. 3m–o, 4a,d). The zonal SR04 section across the Weddell gyre exhibits the most consistent trend among the sections crossing the Weddell–Enderby basin with a water-mass freshening of $\sim 0.05 \times 10^{-3}$ PSS-78 yr^{-1} in the interior and slightly higher values along its east and west flanks, where the deep westward flow of the southern limb of the Weddell gyre and the northward-flowing current carrying recently formed WSBW are found, respectively (Gordon et al. 2010). The heave, however, causes a bottom-intensified salinification of ~ 0.1–0.3×10^{-3} PSS-78 yr^{-1} throughout much of the water column, consistent with a decrease in the volume of WSBW in the basin (PJ12), resulting in a net salinification across most of the section (Fig. 3o). Section A12 (0° longitude; not shown), which cuts meridionally through eastern end of the Weddell gyre, is noisier than SR04 but roughly consistent within errors with the pattern seen along SR04. Farther to the east, section I06 (30°E) across the Enderby Basin shows water-mass freshening of less than 0.1×10^{-3} PSS-78 yr^{-1}, smaller than the measurement error, but again consistent with other lines in this basin, along with a compensating heave of $\sim 0.2 \times 10^{-3}$ PSS-78 yr^{-1} (not shown). Together, these three lines yield a basin-mean salinification of 0.1×10^{-3} PSS-78 yr^{-1}, significantly different from zero at 95% confidence for -0.2°C $< \theta <$ 0.5°C (Fig. 4a).

North of the Weddell–Enderby basin, the Scotia Sea and the Argentine Basin, both fed by AABW from the Weddell Sea and vicinity (Fig. 1), show little bottom water salinity change rising above the noise. SR01 across Drake Passage (not shown) is extremely noisy and we can find no discernible signal. All sections crossing the Argentine Basin show little water-mass change but a slight salinification because of deep isotherm heave (not shown).

Finally, the basin-mean $d\theta/dt$ for all three of the southernmost basins exhibits statistically significant warming trends ranging from 0.002° to 0.005°C yr^{-1} for $\theta <$ 0.5°C (Fig. 4g–i). This trend is comparable to the 0.003°C yr^{-1} warming PJ10 found below 3000 m south of the SAF, only here we have averaged along depths of mean potential isotherms within each basin instead of on isobaths, as done in PJ10. The basin-mean $d\theta/dt$ is more consistent along depths of mean isotherms (Figs. 4g–i

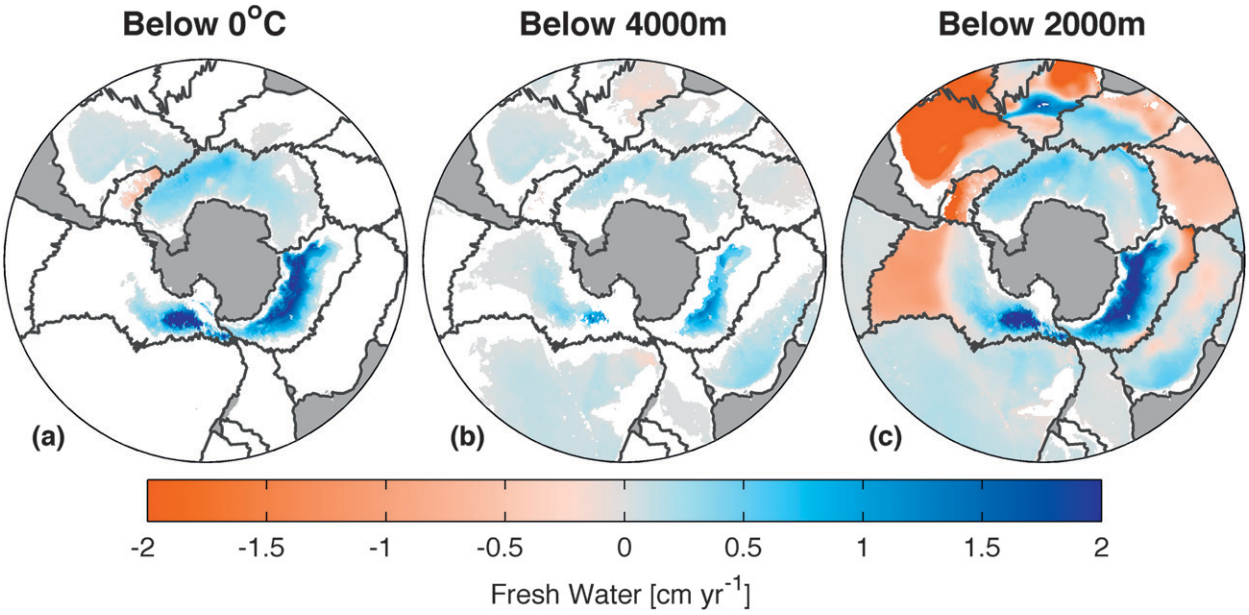

FIG. 5. Local vertical column freshwater fluxes (color; cm yr^{-1}) below (a) 0°C, (b) 4000 m, and (c) 2000 m, equivalent to observed water-mass salinity changes. Basin boundaries (gray lines) and land (gray shading) are shown.

versus Fig. 9d of PJ10), arguably making this new calculation the preferable method.

5. Freshwater, heat, and SLR budgets

Here we apply the basin means (Fig. 4) for water-mass, heave, total S, and θ trends over the entire Southern Ocean, here defined as south of 30°S, to evaluate their contributions to ocean freshwater budgets (section 5a), global heat budgets (section 5b), and SLR (section 5c). For basins and the entire domain, the budget calculations are conducted from the bottom to three upper bounds: climatological $\theta = 0$°C as a rough proxy for the upper boundary of AABW (Foster and Carmack 1976), 4000 m for a deep-ocean estimate where water properties are most strongly influenced by AABW (Johnson 2008; following PJ10), and 2000 m to extended our analysis to the current maximum sampling depth of Argo floats (e.g., Roemmich et al. 2009).

The basin-mean rates and errors are applied to the climatological θ and S fields (Gouretski and Koltermann 2004). The climatological θ and S vertical profiles are put onto a uniform 20-m-depth grid using a shape-preserving piecewise cubic interpolation. Each basin-mean rate and its standard deviation on the θ grid (Fig. 4) are interpolated onto the climatological θ profiles at each horizontal grid point, assigning all four rates and their standard deviations as discussed above. Regions above the CDW θ maximum are not considered here since the method used does not allow it. Given the focus on AABW changes, this limitation is minor.

a. Freshwater budget

Here we quantify the freshwater uptake owing to deep water-mass changes in the deep Southern Ocean, including in AABW, and compare its magnitude to that of the excess mass flux off Antarctica in recent decades from ice melt. We estimate the freshwater flux by calculating the amount of freshwater V_{fw} necessary to add to an initial volume V_i with initial salinity S_i in order to cause the water to freshen at the observed dS_{WM}/dt over a 1-yr period to a final salinity S_f. If salt is conserved and we only change the salinity by adding freshwater to the system to change V_i to a final volume V_f, then V_{fw} is calculated as

$$V_{\mathrm{fw}} = \int V_f - V_i = \int \left(\frac{S_i}{S_f} - 1 \right) dv, \qquad (1)$$

neglecting the relatively small change in density. Here S_i is the gridded climatological salinity (Gouretski and Koltermann 2004) and S_f is calculated by applying dS_{WM}/dt for 1 yr at each climatological grid point. The dv for each grid point is calculated as the volume of the ½° longitude by ½° latitude by 20-m-depth box. Local freshwater fluxes in meters per year are found by integrating in the vertical from the bottom upward to $\theta =$ 0°C, 4000 m, and 2000 m (Fig. 5), and basin totals are found by integrating over the whole basin below these same surfaces (Table 1). The standard deviations of V_{fw} for the basin means are found by applying $S_f \pm 1$

TABLE 1. Freshwater gain (FW; Gt yr^{-1}), SLR (mm yr^{-1}), and heat uptake (TW) with uncertainties at the 95% confidence level below $\theta = 0°C$, 4000 m, and 2000 m in the ABB, AAB, WEB (see Fig. 1), and the whole Southern Ocean south of 30°S (Fig. 1). Freshwater estimates are calculated following (1) using basin-mean freshening trends owing to only water-mass changes. Steric SLR trends are estimated from (3) broken into water-mass, heave, total salinity, and warming trends. The total steric SLR is also given. Heat uptake is calculated following (2) using basin-mean warming trends. Values statistically different from zero at the 95% confidence are given in bold.

		FW (Gt yr^{-1})	SLR (mm yr^{-1})					Heat (TW)
		Water mass	Water mass	Heave	Salinity	θ	Total	θ
Below 0°C	ABB	**25 ± 9**	**0.17 ± 0.06**	0.00 ± 0.02	**0.18 ± 0.07**	**0.31 ± 0.10**	**0.49 ± 0.13**	**1.0 ± 0.3**
	AAB	**48 ± 36**	**0.22 ± 0.16**	**−0.07 ± 0.05**	0.15 ± 0.18	**0.5 ± 0.28**	**0.65 ± 0.33**	**2.5 ± 1.4**
	WEB	24 ± 54	0.05 ± 0.11	−0.12 ± 0.12	−0.07 ± 0.12	**0.66 ± 0.45**	**0.59 ± 0.46**	**7.7 ± 5.3**
	Total *S* of 30°S	**99 ± 56**	**0.09 ± 0.05**	**−0.08 ± 0.04**	0.00 ± 0.06	**0.52 ± 0.17**	**0.52 ± 0.18**	**14 ± 5**
Below 4000 m	ABB	**9 ± 4**	**0.03 ± 0.01**	−0.01 ± 0.01	**0.02 ± 0.02**	**0.18 ± 0.06**	**0.20 ± 0.06**	**1.1 ± 0.3**
	AAB	**17 ± 13**	**0.12 ± 0.1**	−0.02 ± 0.03	**0.11 ± 0.1**	**0.14 ± 0.13**	**0.25 ± 0.17**	**0.4 ± 0.4**
	WEB	10 ± 28	0.03 ± 0.09	−0.05 ± 0.08	−0.02 ± 0.05	**0.30 ± 0.23**	**0.28 ± 0.24**	**1.9 ± 1.5**
	Total *S* of 30°S	**53 ± 21**	**0.02 ± 0.01**	**−0.02 ± 0.01**	0.01 ± 0.01	**0.13 ± 0.05**	**0.14 ± 0.05**	**5 ± 2**
Below 2000 m	ABB	−28 ± 43	−0.05 ± 0.08	0.02 ± 0.07	−0.03 ± 0.08	**0.44 ± 0.26**	**0.41 ± 0.27**	**5.7 ± 3.4**
	AAB	48 ± 66	0.15 ± 0.2	−0.12 ± 0.21	0.03 ± 0.29	**1.03 ± 0.83**	**1.06 ± 0.89**	**8.1 ± 6.7**
	WEB	27 ± 81	0.06 ± 0.17	−0.13 ± 0.19	−0.07 ± 0.2	0.70 ± 0.70	0.63 ± 0.73	7.8 ± 8.0
	Total *S* of 30°S	**−454 ± 241**	**−0.12 ± 0.06**	**0.09 ± 0.07**	−0.03 ± 0.06	**0.37 ± 0.15**	**0.34 ± 0.16**	**34 ± 14**

standard deviation of S_f in (1). The basin DOFs are θ volume-weighted mean along-isotherm DOFs below a given surface (Fig. 4) and the 95% confidence intervals (Table 1) are calculated using Student's t distribution. Finally, a total for the whole Southern Ocean below each top surface is calculated as a sum of all the basin values south of 30°S with 95% confidence intervals found using the sum of the basin standard deviations and DOFs (Table 1). Again, the 95% confidence intervals reflect the spatial variance of the trend estimates and assume that the along-section variability in each basin is representative of that within the entire basin (Table 1).

Local estimates from the bottom to $\theta = 0°C$ show the largest deep freshening occurring in the west Pacific and Indian Ocean sectors (Fig. 5). The local freshwater flux in these regions for $\theta = 0°C$ exceeds 2 cm yr^{-1} over the northwest corner of the Amundsen–Bellingshausen basin and most of the deep portions of the Australian–Antarctic basin (Fig. 5a), despite $\theta < 0°C$ occupying only ~1000–1500 m of the water column. This flux is equivalent to total freshwater additions of 25 ± 9 and 48 ± 36 Gt yr^{-1} into the Amundsen–Bellingshausen and Australian–Antarctic basins, respectively (Table 1), suggesting that a large fraction of the estimated recent 140 Gt yr^{-1} freshwater flux from ice melt (Rignot et al. 2008) may be taken up by freshening AABW.

The Weddell–Enderby basin also shows a slight freshwater flux of 0.5 cm yr^{-1} below $\theta = 0°C$ (Fig. 5). This small amount reflects the very slight observed 0.1×10^{-3} PSS-78 yr^{-1} water-mass freshening (Fig. 4a) applied to the relatively large volume of AABW, with water of $\theta \leq 0°C$ as much as 4000 m in thickness (e.g., Fig. 3m). The relatively large volume of AABW combined with the small water-mass freshening gives an uncertain total freshening of 24 ± 54 Gt yr^{-1}.

Integrating vertically to 4000 and 2000 m further emphasizes the pattern discussed above south of the SAF and shows a strong water-mass salinification in the North Atlantic Deep Water (NADW) north of the SAF at intermediate depths (Fig. 5 and Table 1). Integrating to 4000 m (Fig. 5b), containing only a fraction of $\theta < 0°C$ (Fig. 3: bold black contours), gives a fraction of the freshening seen for $\theta < 0°C$ (Fig. 5a). Integrating to 2000 m (Fig. 5c), the local water-mass freshwater flux south of the SAF is almost identical as that from integrating to the 0°C isotherm, indicating that water-mass freshwater changes are mostly constrained to $\theta < 0°C$ with little water-mass freshening in the waters between 0°C and 2000 m (Figs. 3a,d,g,j). South of the SAF, CDW lies above 2000 m; therefore, none of these isotherms or isobar surfaces reflect changes in CDW south of the SAF. However, north of the SAF between 2000 and 3000 m, in the waters heavily influenced by NADW ($\theta \sim 2.8°C$), a strong salinification is observed, seen as a negative local freshwater fluxes of between −1 and −10 cm yr^{-1} in the local fluxes (Fig. 5c). These waters are also freshening and warming from heave (not shown). The property changes in these regions are separate from the deep AABW changes discussed in this paper and likely indicate physical changes in the NADW in these regions.

b. Heat budget

We find large and statistically significant heat uptake in each basin and the whole Southern Ocean for $\theta < 0°C$, below 4000 m, and below 2000 m (Table 1). The rate of heat gain Q is given by

$$Q = \int \rho C_p \, d\theta/dt \, dv, \tag{2}$$

where density ρ and heat capacity C_p are calculated from the climatological θ, S, and pressure at each grid point. The standard deviation of Q is found by replacing $d\theta/dt$ in (2) with the standard deviations of $d\theta/dt$. We sum the errors because the individual grid points are not independent of each other. The total DOF and 95% confidence intervals for each basin and total Southern Ocean (Table 1) are estimated by previously described methods (section 5a). We find a large, statistically significant heat gain throughout the water column in the Southern Ocean. Totals found here are slightly smaller than PJ10 (discussed further in section 6) but agree within uncertainties.

c. Sea level rise

Changes in density of AABW due to dS_T/dt, dS_{WM}/dt, dS_H/dt, and $d\theta/dt$ contribute to halosteric and thermosteric SLR. We calculate the contribution of each component to SLR using

$$\mathrm{SLR}_{\mathrm{halosteric}} = \frac{\int -\beta \, dS/dt \, dv}{\mathrm{SA}} \quad \text{and}$$

$$\mathrm{SLR}_{\mathrm{thermosteric}} = \frac{\int \alpha \, d\theta/dt \, dv}{\mathrm{SA}}, \tag{3}$$

where the thermal expansion coefficient α and the haline contraction coefficient β are calculated locally from the climatological gridded θ, S, and pressure. For a local estimate, the integral is evaluated vertically from the bottom to a top surface at each grid point where the surface area (SA) has the surface area of that grid point, yielding its contribution to local SLR in millimeters per year (Fig. 6). Again, the top surfaces considered here are $\theta = 0°C$, 4000 m, and 2000 m. For each basin, an average SLR is calculated using (3), where the volume integral is now over the entire region from the bottom to the top surface under consideration and SA is the surface area of that top surface for the basin (Table 1). The gridded standard deviations are integrated again following (3) to estimate the total basin standard deviation. The 95% confidence intervals are estimated assuming Student's t distribution and using the total DOF below a given surface as described in section 5a.

Water-mass freshening tends to reduce SLR in all three southernmost basins while the heave salinification raises SLR (Fig. 6). The local effects of water-mass freshening vary spatially but follow the spatial patterns seen in the freshwater flux (Fig. 5), with the strongest signal seen in the South Pacific and south Indian Oceans (Figs. 6a,e,i). Heave salinification counteracts some of the SLR, except in the Amundsen–Bellingshausen Basin where S is almost constant versus θ in deeper, colder waters (Figs. 6b,f,j and Table 1). The net effect is a slight ($\sim -0.02\,\mathrm{mm\,yr^{-1}}$) local negative SLR in the South Atlantic and a net positive ($\sim 0.03\,\mathrm{mm\,yr^{-1}}$) SLR in the South Pacific and south Indian Ocean sectors of the Southern Ocean (Figs. 6c,g,k and Table 1). In total, the Southern Ocean salinity changes have a near-zero net effect on SLR (Table 1), because of the contribution of salinification in the Weddell–Enderby and Argentine basins almost exactly canceling the contribution of freshening in Australian–Antarctic and Amundsen–Bellingshausen basins. The salinity contribution is smaller than the warming contribution of 1–2 $\mathrm{mm\,yr^{-1}}$ throughout the Southern Ocean (Figs. 6d,h,l and Table 1).

6. Discussion

The Southern Hemisphere has experienced dramatic changes in recent decades owing to increases in atmospheric concentration of greenhouse gases and ozone–depleting chemicals. These changes include increased Southern Ocean warming (Gille 2008), increased glacial melt in the East Antarctic and Antarctic Peninsula (Rignot et al. 2008), a global slowdown of the bottom limb of the MOC (Kawano et al. 2010; Kouketsu et al. 2011; PJ12), and freshening of AABW (Jacobs and Giulivi 2010; Swift and Orsi 2012). Here we have examined property changes in the deep Southern Ocean, distinguishing between changes in the θ–S relation and vertical heave of θ surfaces within and associated with AABW. We conclude with a discussion comparing the amount of warming and freshening estimated in AABW to the net global radiative imbalance, total glacial meltwater runoff from Antarctica, and global-mean SLR.

Freshening of AABW in the Pacific and Indian Ocean sectors of the deep Southern Ocean appears to account for roughly half of the net increase in Antarctic continental ice melt of recent years. The strongest freshening owing to water-mass shifts is seen near the AABW source regions and follows the path of AABW deep circulation in the three southernmost basins (Fig. 5a), reflecting the introduction of a fresher variety of AABW into the deep Southern Ocean. The strongest freshening

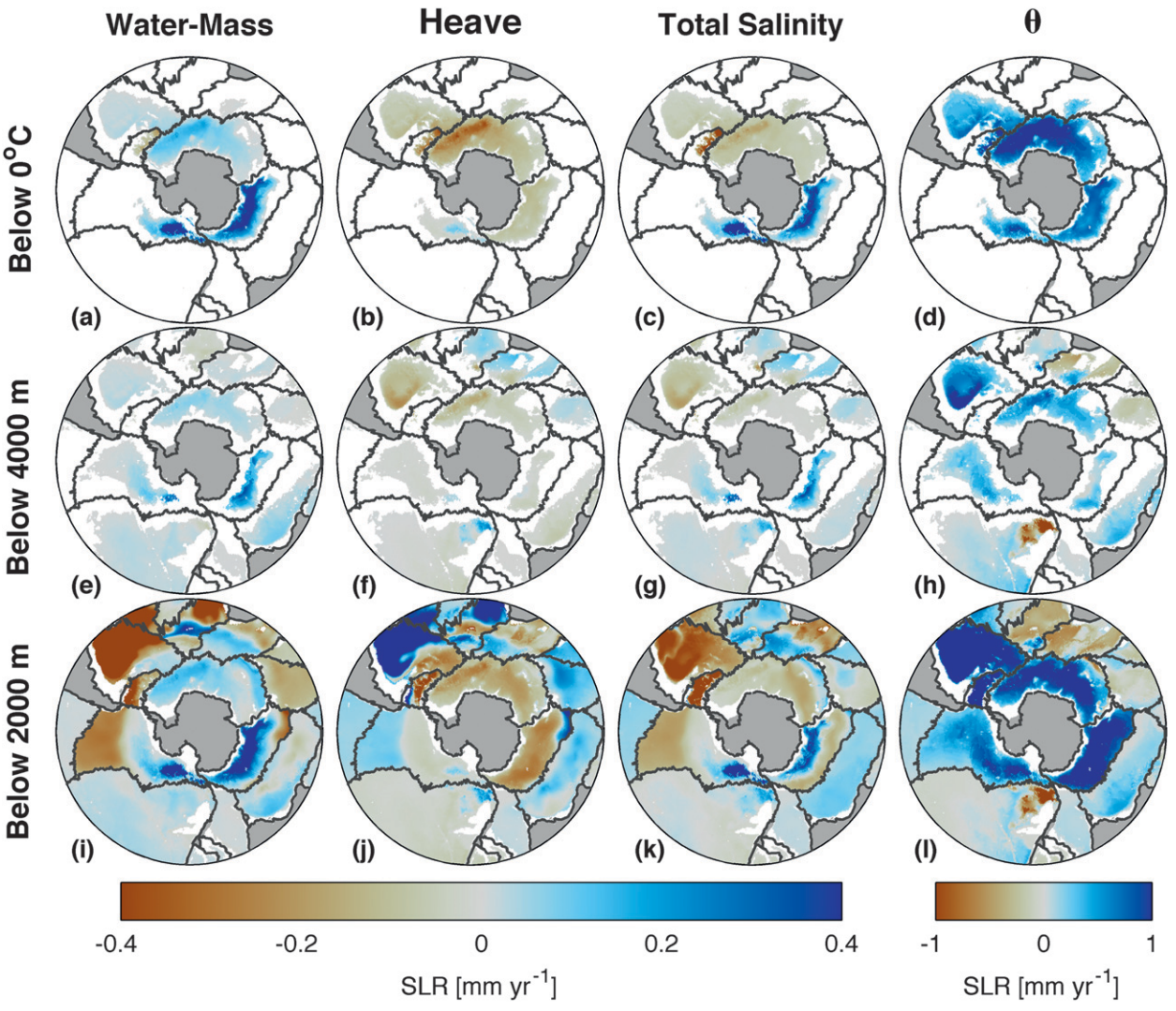

FIG. 6. Vertical column total sea level rise (mm yr^{-1}) below (a)–(d) $\theta = 0°C$, (e)–(h) 4000 m, and (i)–(l) 2000 m owing to (a),(e),(i) water-mass S changes; (b),(f),(j) heave S changes; (c),(g),(k) net S changes; and (d),(h),(l) θ changes. Blue indicates areas of positive SLR and brown indicates areas of negative SLR (see color legends). SLR is calculated based on basin- (gray lines) mean rates of change in S and θ (e.g., Fig. 4) along climatological isotherms (see section 4).

signal in the youngest AABW to the south with no freshening observed in the older AABW farther to the north (Fig. 5) suggests that this freshening flux may have started relatively recently. The Amundsen coast freshwater flux into the South Pacific and south Indian Oceans that freshens the shelf water components of AABW there is probably largely owing to net increase in continental ice melt (Jacobs and Giulivi 2010), estimated to be 140 Gt yr^{-1} over recent decades (Rignot et al. 2008). Our estimates are that the deep Amundsen–Bellingshausen and Australian–Antarctic basins have exhibited increases of 25 ± 9 and 48 ± 36 Gt yr^{-1}, respectively, of freshwater between roughly 1991 and 2008, making the deep ocean a significant sink for the recent increase in glacial melt. The Weddell Basin also exhibits hints of water-mass freshening, albeit at a slower rate that is smaller than the measurement error. However, the spatial pattern of strongest freshening in the newest AABW and the consistency of the freshening throughout the basin (Fig. 3m) suggest that AABW in the Weddell may also be getting fresher.

The heave component of AABW changes found here reflects a loss of volume in AABW over time, seen farther from the source than the advected water-mass freshening signal because production rate changes are communicated by pressure waves on much shorter time scales (e.g., Masuda et al. 2010). PJ12 found an 8-Sv ($1\,Sv \equiv 10^6\,m^3\,s^{-1}$) loss in volume of deep Southern

Ocean water colder than 0°C, suggesting a recent decrease in the production of AABW. Paleoproxies indicate that the bottom limb of the MOC has been in multiple steady states during different climate regimes (Lynch-Stieglitz et al. 2007). Current water-mass volumes and chemistry of the global inventory of AABW versus NADW suggest that past rates of AABW production may have been higher, also supporting the hypothesis of smaller production rates of AABW in recent decades (Broecker et al. 1999; Johnson 2008). Here we separate heave from water-mass changes in the deep ocean and show that, while the water-mass changes are currently limited to the deep basins adjacent to Antarctica, heave is responsible for part of the deep-ocean changes there and most, if not all, of the deep-ocean changes in AABW farther north. Furthermore, the deep volume loss of water colder than 0°C is consistent with the warming and salinification of the water between 0°C isotherm and 1000 m in the south Indian and South Pacific Oceans (Figs. 3b,e,h,k,n).

Further investigation of the relative contribution of heave verses water-mass changes in AABW, including the source of the freshening, could be conducted using chemical tracers such as oxygen, nutrients, $\delta^{18}O$, and chlorofluorocarbons along repeated sections. Temporal changes in these chemical tracers would provide additional information about changes in the age, water properties, and formation rates of the AABW. High-resolution models could also be used to examine the possible mechanisms of AABW changes. However, ocean global circulation models (OGCMs), such as those used for climate projections, do not yet resolve the complex set of processes involved in AABW formation and thus are not yet likely to reproduce accurately observed AABW changes.

AABW warming from heave contributes to the net ocean heat uptake. The earth is currently out of radiative balance because of increasing atmospheric greenhouse gas concentrations. Satellite and in situ measurements show that the earth has been gaining heat at a rate of 183 TW between 1972 and 2008 (Church et al. 2011) with 90% of the excess energy being absorbed by the ocean. For comparison, the 33.8 ± 13.6 TW of warming found here south of 30°S below 2000 m (Table 1) amounts to about 0.07 ± 0.03 W m^{-2} when calculated as a flux over the entire earth surface. This is about 14% of the above total heat uptake.

The values of heat gain we find in the Southern Ocean are generally smaller than those of PJ10 and have smaller confidence intervals. Our mean heat fluxes below 4000 m in the Amundsen–Bellingshausen, Australian–Antarctic, and Weddell–Enderby basins are 0.14 ± 0.04, 0.11 ± 0.11, and 0.23 ± 0.18 W m^{-2}, respectively. Comparable values from PJ10 are 0.20 ± 0.14, 0.32 ± 0.17, and 0.44 ± 0.36 W m^{-2}, respectively. These two sets of estimates agree within confidence limits. While some data have been added for the most recent estimates, much of the difference is due to a change in methods. We now find basin means on mean θ depths and apply them by θ to the climatological-mean θ field instead of doing calculations on isobars. This new method gives smaller heat gains than PJ10 because the large warming in the deep southernmost waters raises the whole basin mean along an isobar, thus raising the basin total when integrated on isobars. When the rates are calculated and applied on θ, the strongest signal is contained geographically to the deep southernmost region, thus giving a more accurate but smaller total heat flux. The 95% confidence intervals are slightly smaller here than in PJ10 partly because we use more data but mostly because the variations across the basin are smaller on mean depths of isotherms than along isobars.

Finally, both the observed heave and water-mass freshening signals in the deep Southern Ocean contribute to SLR (Table 1). Global-mean sea level is estimated to rise at a rate of 3.2 ± 0.4 mm yr^{-1} between 1993 and 2008, with 0.7 ± 0.3 mm yr^{-1} owing to thermal expansion in the upper water column and the rest owing to ice melt, terrestrial water storage changes, and deep-ocean warming (Church et al. 2011). Water property changes south of 30°S for $\theta < 0$°C cause a local-mean SRL of 0.52 ± 0.18 mm yr^{-1} with almost all of this due to changes in θ (Table 1). The heave component, comprised of the sum of +0.52 mm yr^{-1} SLR owing to warming and −0.08 SLR mm yr^{-1} from salinification heave (Table 1), accounts for a SLR of +0.44 mm yr^{-1}. The water-mass freshening causes an additional 0.09 mm yr^{-1}. Therefore, in the deep Southern Ocean, local SLR due to AABW changes is a significant fraction of the global-mean rate of SLR.

Acknowledgments. We thank the hundreds of people who helped to collect, calibrate, process, and archive the WOCE and CLIVAR datasets, without whom global assessments of ocean variability like this one would be impossible. We also thank those who provided us with unreported SSW batch numbers for many cruises. D. Roemmich suggested an improvement for the error analysis. Finally, suggestions of two anonymous reviewers and editor Anand Gnanadesikan improved this manuscript. This work was supported by the NOAA Climate Program Office, NOAA Research, and NASA Headquarters under the NASA Earth and Space Fellowship Program Grant NNX11AL89H.

APPENDIX

Ad Hoc Salinity Adjustments

We attempt to correct for small intercruise salinity biases as offsets for all occupations of repeated hydrographic

TABLE A1. IAPSO SSW batch number with recommended SSW batch salinity offset (Kawano et al. 2006; T. Kawano 2011, personal communication) for each leg listed by WOCE ID (with alternative ID used on http://cchdo.ucsd.edu in parentheses if different) and year. If more than one leg of a section is occupied per year, legs are differentiated by geographical region [east (E), west (W), north (N), south (S), central (C), or Antarctic (A)] or, if an exact repeat of a leg is done twice in 1 yr, then legs are listed chronologically by the date of the first station occupied. If no SSW batch number is listed, we were unable to determine this information from cruise reports or through personal queries to data originators. As of September 2012, there is no known offset for batch numbers P113 and P152; therefore, no SSW batch offset is applied for cruises using those SSW batches. The last column lists the additional ad hoc salinity offsets estimated by and applied for our analyses (see appendix). If legs do not have an ad hoc salinity offset listed, then one was not possible to estimate owing to the section location or length. Both offsets are added to salinity data.

WOCE ID	Year	SSW batch number	SSW offset (×1000)	Ad hoc offsets (×1000)
A01(AR07)E	1990	P112	1.9	0.186
A01(AR07)W	1990	P104	1.1	—
A01(AR07)E	1991	P112/P114	1.9/2	—
A01E	1991	P112	1.9	−0.289
A01(AR07)E	1992	P119	0	−0.836
A01(AR07)W	1992	P112	1.9	—
A01(AR07)W	1993	P117	—	—
A01(AR07)E	1994	—	—	—
A01(AR07)W	1994	P123	0.7	—
A01W	1994	P124	0.6	−0.496
A01(AR07)E	1995	—	—	−0.551
A01W	1995	P126	0.6	—
A01(AR07)E	1996	—	—	1.870
A01(AR07)W	1996	P124	0.6	—
A01(AR07)E	1997	P129	0.4	—
A01(AR07)W	1997	P129	0.4	—
A01(AR07)W	1998	P133	0.3	—
A02	1994	P124	0.6	−1.849
A02	1997	P129	0.4	1.849
A05	1981	P93	0.9	−2.867
A05	1992	P120	−0.9	0.114
A05(AR01)	1998	P125	0.2	0.259
A05	2004	P143/P144	−0.2/−0.5	1.028
A05	2010	—	—	1.952
A10	1992	P120	−0.9	−1.110
A10	2003	P142	0.2	0.134
A10	2011	P152	—	0.829
A12	1992	P114	2	−0.553
A12(S04)	1996	P127	0.8	0.437
A12	1999	P134	0.3	−0.038
A12	2000	P135	0.2	0.624
A12	2002	P140	−0.3	−0.034
A12	2005	P144	−0.5	0.273
A13.5	1983	P92	−0.2	−1.276
A13.5	2010	P147	−0.5	1.276
A16N	1988	P108	1.7	0.587
A16C	1989	P108	1.7	−0.494
A16S	1989	P108	1.7	0.435
A16	1993	P119	0	−0.869
A16(A23)	1995	P125	0.2	0.332
A16(AR21)	1998	P133	0.3	0.166
A16	2003	P143	−0.2	−0.384
A16	2005	P143	−0.2	0.087
A16	2011	—	—	2.276
A20	1997	P131	0.1	−1.446
A20	2003	P140	−0.3	1.446
A22	1997	P131	0.1	−0.283
A22	2003	P140	−0.3	0.283
I02	1995	P128	1.4	0.246
I02	2000	P133/P138	0.3/−0.1	−0.246

TABLE A1. (*Continued*)

WOCE ID	Year	SSW batch number	SSW offset (×1000)	Ad hoc offsets (×1000)
I03	1995	P126	0.6	0.328
I03	2003	P142	0.2	−0.328
I04	1995	P126	0.6	−0.274
I04	2003	P142	0.2	0.274
I05	1987	P97	2.1	−1.406
I05W	1995	P126	0.6	0.836
I05E	1995	P126	0.6	0.449
I05	2002	P140	−0.3	1.031
I05	2009	P149	0.8	0.234
I06	1993	P121	0.4	−0.264
I06	1996	—	—	−0.042
I06	2008	—	—	0.186
I08S	1994	P124	0.6	−0.802
I08(I09N)N	1995	P126	0.6	0.479
I08	2000	P133/P138	0.3/−0.1	−0.564
I08(I09N)N	2007	P147	−0.5	0.206
I08S	2007	P147	−0.5	0.802
I09	1995	P124	0.6	−0.338
I09(S03)S	1995	P121/P123	0.4/0.7	—
I09	2004	P141	−0.3	0.338
IR6	1995	—	—	0.597
IR6	1995	—	—	0.828
IR6(I02)	2000	P133/P138	0.3/−0.1	−1.339
P01	1985	P96	2.5	1.154
P01C	1999	P135	0.2	−0.680
P01E	1999	P133/P134	0.3/0.3	0.386
P01H	1999	P135	0.2	—
P01W	1999	P133	0.3	−0.849
P01C	2007	P148	0.2	−0.304
P01W/E/H	2007	P148	0.2	−0.651
P02	1985	P96	2.5	0.956
P02E	1993	P123	0.7	1.175
P02	1994	P144	−0.5	−1.968
P02C	1994	P121	0.4	−2.600
P02W	1994	P144	−0.5	4.534
P02	2004	P144	−0.5	0.274
P03	1985	P96	2.5	1.764
P03E	2005	P145	−0.8	−1.553
P03W	2005	P145	−0.8	−2.009
P03	2006	P145	−0.8	—
P06C	1992	P116	1.4	−1.205
P06E	1992	P116	1.4	0.357
P06W	1992	P116	1.4	−1.167
P06W	2003	P142	0.2	0.358
P06E	2003	P142	0.2	−0.837
P06	2009	—	—	0.866
P09	1994	P123	0.7	−0.200
P09	2010	P152	—	0.200
P10	1993	P114/P120	2/−0.9	0.323
P10	2005	P145	−0.8	−0.323
P14	1992	P120	−0.9	0.087
P14	1993	P122	0.4	0.571
P14N	2007	P148	0.2	−0.777
P14S	2007	P148	0.2	−0.376
P15	1996	P114	2	−1.304
P15	2001	P140	−0.3	0.840
P15	2009	P148/P150	0.2/0.8	0.490
P16	1984	P92	−0.2	2.901

TABLE A1. (*Continued*)

WOCE ID	Year	SSW batch number	SSW offset (×1000)	Ad hoc offsets (×1000)
P16C	1991	P114	2	0.932
P16N	1991	P110	1.9	−1.431
P16S	1991	P108/P114	1.7/2	0.010
P16A	1992	P120	−0.9	0.222
P16S	2005	P144	−0.5	−0.319
P16N	2006	P145	−0.8	−1.141
P17S	1991	P108/P114	1.7/2	−0.512
P17C	1991	P120	−0.9	2.470
P17A	1992	P120	−0.9	0.460
P17N	1993	P122	0.4	0.915
P17	2001	P139	0.4	−1.754
P18S	1994	P114	2	−0.209
P18N	1994	P114	2	0.335
P18(AAIW)	2006	P146	−1.2	—
P18N	2007	P147	−0.5	−0.483
P18S	2008	P147	−0.5	0.209
P21W	1994	P123	0.7	−0.447
P21E	1994	P123	0.7	−0.240
P21	2009	P150	0.8	0.396
S01	1993	—	—	—
S01	1994	—	—	—
S01	1996	—	—	—
SR03	1991	P115	2.5	—
SR03	1993	P121	0.4	−5.643
SR03	1994	P121/P123/P137/P140	0.4/0.7/−0.4/−0.3	0.206
SR03(S03)	1995	P121/P123	0.4/0.7	−0.997
SR03	1995	P128/P130	1.4/0.3	3.454
SR03	1996	P128/P130	1.4/0.3	1.606
SR03	2001	P113/P133/P137/P140	—/0.3/−0.4/−0.3	1.385
SR03	2008	P140/P147/P148	−0.3/−0.5/0.2	0.884
S04	1989	P111	2.1	−0.703
S04	1990	P113	—	1.523
S04	1992	—	—	0.667
S04	1996	P127/P148	0.8/0.2	−1.893
S04	1998	P113	—	0.995
S04	2005	P144	−0.5	−0.716
S4P	1992	P108	1.7	0.059
S4P	2011	P152	—	−0.059

sections (Table A1; see PJ12 for full dataset description). We estimate these offsets by comparing S data in select geographical regions containing old, well-mixed, low-variability water, where the adjective ''old'' denotes a long time since the water was last in contact with the atmosphere. These small intercruise S biases can arise from differences in sampling, measuring, and calibration routines conducted by different personnel.

Intercruise S offsets are identified for all occupations of every section. First, each cruise is divided into subsections based on topographic and dynamic boundaries (such as fronts). Areas near boundaries, strong currents, or water-mass fronts are excluded. For each occupation at each location along a section, the S data are linearly interpolated onto to a 0.01°C-resolution θ grid. The intercruise difference in S (ΔS) is calculated at each θ and each location along the section by subtracting the mean S of all the collocated occupations from each individual occupation. A mean ΔS_{mean} and variance ΔS_{var} are calculated for each subsection along θ surfaces. Within each subsection, a 0.1°C-thick layer is chosen balancing where ΔS_{var} is small and the waters are oldest, as determined by examination of the chlorofluorocarbon, oxygen, nitrate, and Δ^{14}C distributions for the WOCE occupation of each section using the WOCE atlases (e.g., Orsi and Whitworth 2005). These portions of the water column are chosen to maximize the likelihood that ΔS estimates are owing to cruise measurement biases, not physical changes. The weighted means of ΔS_{mean}, $\Delta\overline{S}_{\text{mean}}$, within the selected isotherm bands are found using the inverses of ΔS_{var} for weights. Similarly, the weighted means of ΔS_{var}, $\Delta\overline{S}_{\text{var}}$, are found using

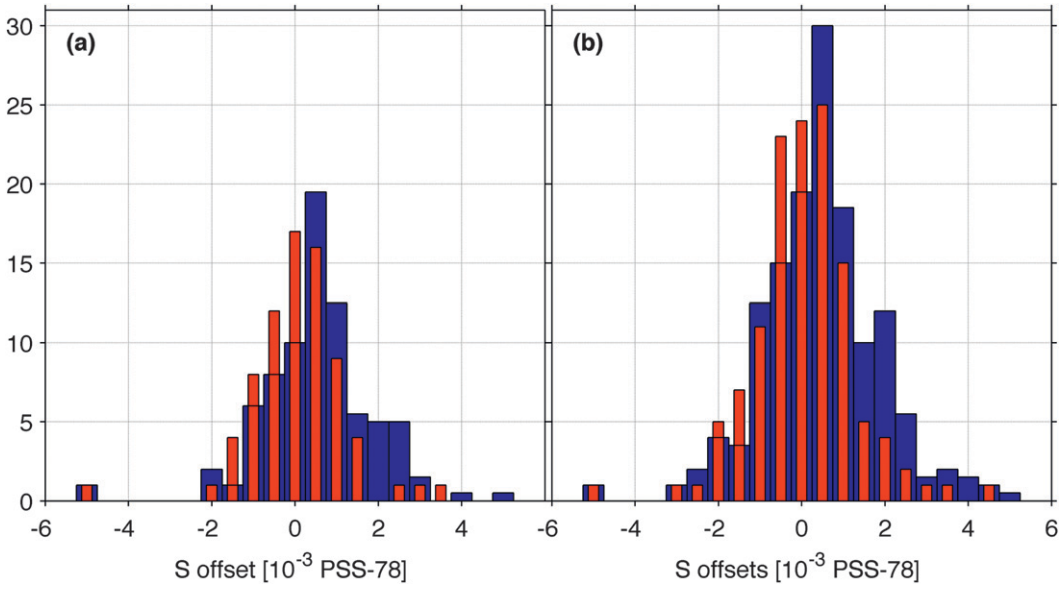

FIG. A1. Histogram of estimated ad hoc salinity offsets (red) and the sum of recommended SSW batch and ad hoc salinity offsets (blue) applied to the CTD data along hydrographic legs in the (a) Southern Ocean and (b) World Ocean (Table A1). If a leg had more than one SSW batch offset, each offset is given an equal weight in computing a mean.

ΔS_{var} as weights. Finally, the S offset for an entire cruise is calculated as the $\Delta\overline{S}_{\text{var}}$ weighted mean of $\Delta\overline{S}_{\text{mean}}$ (Table A1).

The global array of repeated hydrographic sections collected through WOCE and GO-SHIP programs are considered here, consisting of 33 lines with a total of 146 legs collected between 1981 and 2012. SSW batches and their recommended SSW offsets (Kawano et al. 2006; T. Kawano 2011, personal communication) are noted along with the additional ad hoc offset found here (Table A1). Offsets are added to salinity data to obtain the final value. SSW batch offsets are available for 91% of the legs, with missing values either because the SSW batch used is too new for an offset to be estimated or because the SSW batch used is unknown. Additional ad hoc offsets are found for 87% of the legs, with the missing offsets owing to the leg length being too short or the absence of a location on the section suitable to identify an offset. Of the 132 net offsets, 118 are less than the stated CTD salinity accuracy of 0.002 PSS-78, with the mean magnitude of the offsets being 0.0008 PSS-78 (Fig. A1). While the application of SSW batch offsets improves the agreement among occupations of each section, it does not eliminate the need for ad hoc offsets to reduce intercruise salinity biases (Fig. A1).

While these offsets are small, they are important for sea level rise estimates. For example, a 0.002 PSS-78 increase in S applied 1000 m of a 0°C, 34.6 PSS-78 column of water results in a 0.14-mm decrease in SLR compared to only a 0.03-mm SLR increase from a 0.002°C increase in temperature. In addition, the observed freshening between sequential cruises ~10 yr apart ranges from zero to one order of magnitude greater than the WOCE stated salinity accuracy, but the observed warming is one to two orders of magnitude greater than the WOCE temperature accuracy.

REFERENCES

Aoki, S., S. R. Rintoul, S. Ushio, S. Watanabe, and N. L. Bindoff, 2005: Freshening of the Adélie Land Bottom Water near 140°E. *Geophys. Res. Lett.,* **32,** L23601, doi:10.1029/2005GL024246.

Bindoff, N. L., and T. J. McDougall, 1994: Diagnosing climate change and ocean ventilation using hydrographic data. *J. Phys. Oceanogr.,* **24,** 1137–1152.

Broecker, W. S., S. Sutherland, and T. H. Peng, 1999: A possible 20th-century slowdown of Southern Ocean deep water formation. *Science,* **286,** 1132–1135, doi:10.1126/science.286.5442.1132.

Church, J. A., and Coauthors, 2011: Revisiting the earth's sea-level and energy budgets from 1961 to 2008. *Geophys. Res. Lett.,* **38,** L18601, doi:10.1029/2011GL048794.

Coles, V. J., M. S. McCartney, D. B. Olson, and W. M. Smethie Jr., 1996: Changes in Antarctic Bottom Water properties in the western South Atlantic in the late 1980s. *J. Geophys. Res.,* **101,** 8957–8970.

Fahrbach, E., M. Hoppema, G. Rohardt, M. Schroder, and A. Wisotzki, 2004: Decadal-scale variations of water mass properties in the deep Weddell Sea. *Ocean Dyn.,* **54,** 77–91.

——, ——, ——, O. Boebel, O. Klatt, and A. Wisotzki, 2011: Warming of deep and abyssal water masses along the Greenwich meridian on decadal time scales: The Weddell gyre as a beat buffer. *Deep-Sea Res. II,* **58,** 2509–2523, doi:10.1016/j.dsr2.2011.06.007.

Foster, T. D., and E. C. Carmack, 1976: Frontal zone mixing and Antarctic Bottom Water formation in the southern Weddell Sea. *Deep-Sea Res. Oceanogr. Abstr.,* **23,** 301–317.

Fukasawa, M., H. Freeland, R. Perkins, T. Watanabe, H. Uchida, and A. Nishima, 2004: Bottom water warming in the North Pacific Ocean. *Nature,* **427,** 825–827.

Gille, S. T., 2008: Decadal-scale temperature trends in the Southern Hemisphere ocean. *J. Climate,* **21,** 4749–4765.

Gordon, A. L., 1972: Spreading of Antarctic Bottom Waters, II. *Studies in Physical Oceanography—A Tribute to George Wust on His 80th Birthday,* A. L. Gordon, Ed., Gordon and Breach, 1–17.

——, B. Huber, D. McKee, and M. Visbeck, 2010: A seasonal cycle in the export of bottom water from the Weddell Sea. *Nat. Geosci.,* **3,** 551–556, doi:10.1038/ngeo916.

Gouretski, V. V., and K. P. Koltermann, 2004: WOCE global hydrographic climatology. Berichte des Bundesamtes für Seeshifffahrt und Hydrographie 35, 52 pp. + 2 CD-ROMs.

Jacobs, S. S., 2004: Bottom water production and its links with the thermohaline circulation. *Antarct. Sci.,* **4,** 427–437, doi:10.1017/S095410200400224X.

——, and C. F. Giulivi, 2010: Large multidecadal salinity trends near the Pacific–Antarctic continental margin. *J. Climate,* **23,** 4508–4524.

Johnson, G. C., 2008: Quantifying Antarctic Bottom Water and North Atlantic Deep Water volumes. *J. Geophys. Res.,* **113,** C05027, doi:10.1029/2007JC004477.

——, and S. C. Doney, 2006: Recent western South Atlantic bottom water warming. *Geophys. Res. Lett.,* **33,** L14614, doi:10.1029/2006GL026769.

——, S. Mecking, B. M. Sloyan, and S. E. Wijffels, 2007: Recent bottom water warming in the Pacific Ocean. *J. Climate,* **20,** 5365–5375.

——, S. G. Purkey, and J. L. Bullister, 2008: Warming and freshening in the abyssal southeastern Indian Ocean. *J. Climate,* **21,** 5353–5365.

Joyce, T. M., 1991: Introduction to the collection of expert reports compiled for the WHP program. WOCE Hydrographic operations and methods, WOCE Operations Manual, WHP Office Rep. WHPO-91-1, WOCE Rep. 68/91, 4 pp.

Kawano, T., M. Aoyama, T. Joyce, H. Uchida, Y. Takatsuki, and M. Fukasawa, 2006: The latest batch-to-batch difference table of standard seawater and its application to the WOCE onetime sections. *J. Oceanogr.,* **62,** 777–792.

——, T. Doi, H. Uchida, S. Kouketsu, M. Fukasawa, Y. Kawai, and K. Katsumata, 2010: Heat content change in the Pacific Ocean between the 1990s and 2000s. *Deep-Sea Res. II,* **57,** 1141–1151, doi:10.1016/j.dsr2.2009.12.003.

Kouketsu, S., and Coauthors, 2011: Deep ocean heat content changes estimated from observation and reanalysis product and their influence on sea level change. *J. Geophys. Res.,* **116,** C03012, doi:10.1029/2010JC006464.

Lumpkin, R., and K. Speer, 2007: Global ocean meridional overturning. *J. Phys. Oceanogr.,* **37,** 2550–2562.

Lynch-Stieglitz, J., and Coauthors, 2007: Atlantic meridional overturning circulation during the last glacial maximum. *Science,* **316,** 66–69, doi:10.1126/science.1137127.

Masuda, S., and Coauthors, 2010: Simulated rapid warming of abyssal North Pacific water. *Science,* **329,** 319–322, doi:10.1126/science.1188703.

McDonagh, E. L., H. L. Bryden, B. A. King, R. J. Sanders, S. A. Cunningham, and R. Marsh, 2005: Decadal changes in the south Indian Ocean thermocline. *J. Climate,* **18,** 1575–1590.

Meredith, M. P., A. C. Naveira Garabato, A. L. Gordon, and G. C. Johnson, 2008: Evolution of the deep and bottom water of the Scotia Sea, Southern Ocean, during 1995–2005. *J. Climate,* **21,** 3327–3343.

Orsi, A. H., and T. Whitworth II, 2005: *Southern Ocean.* Vol. 1, *Hydrographic Atlas of the World Ocean Circulation Experiment (WOCE),* M. Sparrow. P. Chapman, and J. Gould, Eds., International WOCE Project Office, 223 pp.

——, G. C. Johnson, and J. L. Bullister, 1999: Circulation, mixing and production of Antarctic Bottom Water. *Prog. Oceanogr.,* **43,** 55–109.

Purkey, S. G., and G. C. Johnson, 2010: Warming of global abyssal and deep Southern Ocean waters between the 1990s and 2000s: Contributions to global heat and sea level rise budgets. *J. Climate,* **23,** 6336–6351.

——, and ——, 2012: Global contraction of Antarctic Bottom Water between the 1980s and 2000s. *J. Climate,* **25,** 5830–5844.

Rignot, E., and S. S. Jacobs, 2002: Rapid bottom melting widespread near Antarctic ice sheet grounding lines. *Science,* **296,** 2020–2023, doi:10.1126/science.1070942.

——, J. L. Bamber, M. R. van Den Broeke, C. Davis, Y. Li, W. Jan Van De Berg, and E. van Meijgaard, 2008: Recent Antarctic ice mass loss from radar interferometry and regional climate modeling. *Nat. Geosci.,* **1,** 106–110, doi:10.1038/ngeo102.

Rintoul, S. R., 2007: Rapid freshening of Antarctic Bottom Water formed in the Indian and Pacific oceans. *Geophys. Res. Lett.,* **34,** L06606, doi:10.1029/2006GL028550.

Robertson, R., M. Visbeck, A. L. Gordon, and E. Fahrbach, 2002: Long-term temperature trends in the deep waters of the Weddell Sea. *Deep-Sea Res. II,* **49,** 4791–4806.

Roemmich, D., and Coauthors, 2009: The Argo program: Observing the global oceans with profiling floats. *Oceanography,* **22,** 34–43.

Shepherd, A., D. J. Wingham, and J. A. D. Mansley, 2002: Inland thinning of the Amundsen Sea sector, West Antarctica. *Geophys. Res. Lett.,* **29,** doi:10.1029/2001GL014183.

——, ——, and E. Rignot, 2004: Warm ocean is eroding West Antarctic Ice Sheet. *Geophys. Res. Lett.,* **31,** L23402, doi:10.1029/2004GL021106.

Shimada, K., S. Aoki, K. I. Ohshima, and S. R. Rintoul, 2012: Influence of Ross Sea Bottom Water changes on the warming and freshening of the Antarctic Bottom Water in the Australian-Antarctic Basin. *Ocean Sci.,* **8,** 419–432, doi:10.5194/os-8-419-2012.

Swift, J. H., and A. H. Orsi, 2012: Sixty-four days of hydrography and storms: RVIB *Nathaniel B. Palmer's* 2011 S04P cruise. *Oceanography,* **25,** 54–55, doi:10.5670/oceanog.2012.74.

Whitworth, T., III, 2002: Two modes of bottom water in the Australian-Antarctic Basin. *Geophys. Res. Lett.,* **29,** 1073, doi:10.1029/2001GL014282.

Zenk, W., and E. Morozov, 2007: Decadal warming of the coldest Antarctic Bottom Water flow through the Vema Channel. *Geophys. Res. Lett.,* **34,** L14607, doi:10.1029/2007GL030340.